Hao Chen[1], Hongxing Li[1], Mingjun Wang[1], Yang Pang[1], Hanbing Ai[1], Dequan Hong[2],Hua Zhang[1], Rubing Han[3]

[1]State Key Laboratory of Nuclear Resources and Environment, East China University of Technology, Nanchang, China.

[2]Mengcheng National Geophysical Observatory, Anhui Earthquake Administration, Mengcheng, China

[3]Department of Mathematical Sciences, Tsinghua University, Beijing, China

Correspondence to:

H.X.Li,

lihongxingniran@163.com

Key Points:

- The prediction of the Moho information from receiver functions seismogram by using multi-task deep learning
- The recombining synthetic receiver functions via the style transfer technique
- The early Cretaceous extensional tectonics relics preserved in the lower crust of the Tanlu fault zone and adjacencies

Abstract

We propose a novel scheme that applies a multitasking convolutional neural network to learn the back azimuthal behavior from receiver function seismograms, which can effectively predict the depth and occurrence of the Moho beneath a single seismic station. Our scheme consists of three main steps: 1. Based on the style transfer technique, we generate 9000 synthetic receiver function seismograms blended by realistic noise as training data sets. 2. A multitasking convolutional neural network is trained to predict the depth and occurrence of the Moho. 3. All real receiver function seismograms are reconstructed by the accelerated joint iterative method before prediction. We apply the scheme to study the middle-southern of the Tanlu fault zone and adjacent regions and successfully achieve the depth and occurrence of the Moho beneath 10 permanent seismic stations. The predicted depths are in agreement with the results computed by conventional methods, and the predicted strikes and dip angles present an undulating Moho with near NE-striking. Moreover, the predicted strikes are nearly consistent with the strikes of the normal faults in the upper crust, which implies that intense continental extension in the Cretaceous play a prominent role in the tectonic deformation of the brittle upper crust and the ductile lower crust simultaneously. Besides, it helps to illustrate that the stress field orientation of the major geological event can be recorded and preserved in the lower crust.

Plain Language Summary

We cast the structural study of the Moho with the conventional receiver function method as a deep learning problem. The focus of this paper, subsequently, is placed on the applications of our scheme to real data recorded from 10 permanent seismic stations located in the middle-southern segment of the Tanlu fault zone and its adjacencies. Yielded predicted information reveals an undulating Moho with near NE-striking below the study area, which is rarely unveiled by other traditional approaches. Those tectonics seem to have strong correlations with the Cretaceous continental extension. Meanwhile, our scheme provides an effective way to study other tectonic areas.

1 Introduction

Receiver functions (RFs) are time series to study the structure of the Earth and internal boundaries. As its derivative methods, the H-kappa stacking (Li et al., 2019; Zhu & Kanamori, 2000) is widely used to estimate crustal thickness and ratio of P to S velocities, and the common conversion point stacking (Kosarev et al., 1999; Zhu, 2000) and the migration (eg. Chen et al., 2005; Millet et al., 2019) provide some ways for imaging of the deep interface structure along the profile. Besides, in the single station seismogram with RFs arranged in back azimuth, dipping Moho can often induce the variation of amplitudes and arrivals of the conversions (Ps) and the multiples (PsPs+PpSs, PpPs) (Frederiksen & Bostock, 1999; Langston, 1977; Peng & Humphreys, 1997; Savage, 1998; Zhang & Langston, 1995). Under some circumstances (high signal-to-noise ratio or lower anisotropy), researchers can even analyze the back azimuthal behavior of the phases to recognize the occurrence of the interface qualitatively (eg. Monsalve et al. 2019; Sherrington et al. 2004; Wirth & Long, 2012;). However, the noise contamination and significant anisotropy make the back azimuthal behavior complicated and illegible (Liu & Niu, 2012; McNamara & Owens, 1993; Nagaya et al. 2008). For most existing seismological imaging methods, the stacking and smoothing technique likely tend to erase tectonic features to some extent, and the imaging resolution significantly reduces with the depth increases, resulting in relatively poor observation. In our study, utilizing the powerful feature extraction capability of the multitasking convolutional neural network, we put forward a new deep learning scheme to predict the depth and occurrence of the Moho beneath a single seismic station from the RFs seismogram. The predicted results effectively elucidate structural characteristics of the Moho and indirectly provide new evidence about lower crustal evolution.

Over the last few years, machine learning has been massively adapted to assist the investigation of deep earth structures. Nevertheless, the previous combining study of machine learning and RFs focused mainly on denoising (Dalai et al., 2022) and auto-picking (Gan et al., 2021; Li et al., 2021), rather than delineating structural information of the subsurface. Recently, researchers have begun to realize the potential of combining the two methods. Zhang et al. (2019) reconstructed RFs with PCA to gain a more accessible analysis to the back azimuthal behaviors and the phases. Yang et al. (2022) designed a convolutional neural network to predict the shear wave velocity. Wang et al. (2022) achieved

a substitute method of the H-kappa by deep learning. In this paper, we mainly focus on retrieving the structural information (depth, strike, and dip angle) of the Moho from RFs seismogram using a multitasking convolutional neural network, and more importantly, the findings will provide essential insights into the relationship between the tectonics and geological evolution.

Using broadband data from 10 permanent seismic stations, we applied the newly proposed scheme to study the Tanlu fault zone, a suture between the North China block (NCB) and the Lower Yangtze block (LYZB). The predecessors have researched the deep structure of the TLFZ and its adjacencies over a long period via geophysical methods and found massive shreds of evidence on crustal thickness and structure (Chen et al., 2006; Lei et al.,2020; Lü et al., 2015; Ma et al., 2020; Shi et al., 2013; Ye et al., 2019; Zhang et al., 2020). In the meantime, the geochemical and geological researches also unveil more details on evolution and mechanism (Jia et al., 2016; Kang et al., 2021; Wang et al., 2021; Yin et al., 2020; Zhao et al. 2014; Zheng et al, 2018; Zhu et al. 2018). Despite all this, a current burning issue in geosciences lies in identifying the relation between deep deformation and the evolutional process. Our scheme simultaneously extracts the depth and occurrence of the Moho beneath the stations on the middle-southern segment of TLFZ and adjacent regions. Finally, we will discuss the correlation between lower crustal deformation and geological evolution.

We chose the middle-southern segment of the TLFZ and its adjacencies for scheme testing for two reasons. 1. The study area developed typical thin-skinned tectonics in Eastern China, which indicate a simpler deep geologic structure compared with the thick-skinned structures in Southwest China or double Moho in Tibetan Plateau (Shen et al., 2017; Ye et al., 2015). 2. Previous studies have revealed that the study area has a thin crust (<40 km) and weak velocity anisotropy, which results in RFs with earlier arrival times and explicit behaviors of the phases. Hence this area can be viewed as an ideal place for scheme testing.

2 Methodology

2.1 The style transfer technique

The success of supervised learning depends heavily on the availability and quality of a large volume of sample data and the accuracy of labels. However, unfortunately, on the one hand, the RFs from the bandpass waveform are costly, and the missing traces in partial back azimuth will further degrade the performance of the involved methods. Except for this, the geological distinction between different areas shapes the heterologous features of RFs, which means that a network by simply training observed data from one place will bring about the failure of prediction for another place. On the other hand, the realistic RFs are often contaminated with the noise of different sources, resulting in the disorder of back-azimuthal information of phases and further erroneous identification.

Considering the merits of synthetic data in enlarging sample space and providing an accurate representation of wave propagation, we adopt the synthetic RFs as the training sample set in this work. Besides, we introduce a practical way to

simulate a high-quality synthetic RFs seismogram with noise, namely, using a style transfer technique based on the convolutional neural network (Gatys et al., 2016) to capture noise features from the real data and further integrate them into the synthetic RFs. In this way, the synthetic RFs for training will obtain similar noise levels and characteristics as the real data.

A pre-train VGG-19 network is responsible for separating and recombining the content (the synthetic RFs seismograms without noise) and the style (the noises trimmed from the real RFs), and outputting the recombination (the synthetic RFs seismograms with noise). The outputs of selected specific matching layers are used to define different loss functions, then the final recombining seismogram is calculated iteratively via batch gradient descent.

For the content representation, the content loss is defined as follows:

1

represents the synthetic RFs seismogram, andrepresents recombining RFs seismogram in each iteration. the content representation in a layerof VGG-19 net are stored in a matrix, where is the activation of thefilter at positionin layer. Similarly, the recombined representation on a layerof VGG-19 net are stored in a matrix.

For the style representation, we need to define a feature correlation, given by the Gram matrix, where is the inner product between the vectorised feature mapsandin layer:

2

where represents VGG-19 block. The style loss is defined as follow:

3

In equation (3),represents the style and its matrix size is the same as.is the number of the filters in layer andis filter size.is the style feature representation in layerof VGG-19 net.is weighting factors of the contribution of each layer to the total loss.

Then, the total loss is defined as below:

4

where and are the weighting factors for the content and the style, respectively.

2.2 The multi-task learning based on the hard parameter sharing

We select the most classical and common approach, the hard parameter sharing (Caruana, 1993), to design a multitasking deep neural network. All tasks generally share the hidden layers on the bottom of the network, while the individual task has self-task-specific layers on top of the network. The most significant advantage of this method is that this structure dramatically reduces the risk of overfitting and enhances the robustness of the model (Baxter, 1997; Ruder,

2017). In our deep neural network, the hard share bottom consists of multi-convolutional layers, sharing all learned weights and biases. The output of the hard share bottom as the input is fed into different task-specific layers. We divide our predictive goals into three tasks: the Moho depth is a classification task, while the strike and the dip angle are viewed as two individual regression tasks.

For the Moho depth prediction, we adopt the cross-entropy loss function as follows:

5

Wherepresents the real probability of thedepth class , represents the predictive probability of thedepth class.

The mean squared error loss with L1_L2 class regularization for two regression tasks is calculated as.

6

whereis the number of the RFs samples,is the wights of the layer, andis the regularization parameter.presents the label of theRFs sample, andis the corresponding prediction. Furthermore, the total loss function is a linear combination of loss functions of the three tasks.

2.3 The reconstruction of RFs seismogram via the accelerated joint iterative method

In a realistic RFs seismogram, the uneven distribution of seismic events and the existence of bad traces generally bring about the missing traces in partial back azimuth, so it is necessary to restore and reconstruct RFs seismogram before the prediction. We introduce a sophisticated method derived from the compressive sensing theory (Donoho et al., 2006), the accelerated joint iterative method (AJIM) (Zhang et al., 2022), to reconstruct realistic RFs seismogram based on the acceleration linearized Bregman method (ALBM) (Gou et al., 2014; Huang et al., 2013; Osher et al., 2005) and the iterative shrinkage thresholding algorithm (ISTA) in the curvelet transform domain, where the curvelets as a superior sparse to provide an optimally sparse representation of objects with edges and wave propagators (Candès & Demanet, 2004; Zhang et al., 2017). Moreover, a new exponential function (Zhang et al., 2022) is used to control the contribution of ISTA and ALBM in AJIM. This method can perfectly solve the reconstruction of RFs seismogram with missing traces in partial back azimuth in most cases.

3 Scheme

Based on the methods introduced above, we propose a novel scheme for predicting the depth and occurrence of the Moho. The whole workflow can be observed in Fig. 1. The scheme has good generality and flexibility, which means it can be directly employed in other studying areas with minor and suitable modifications.

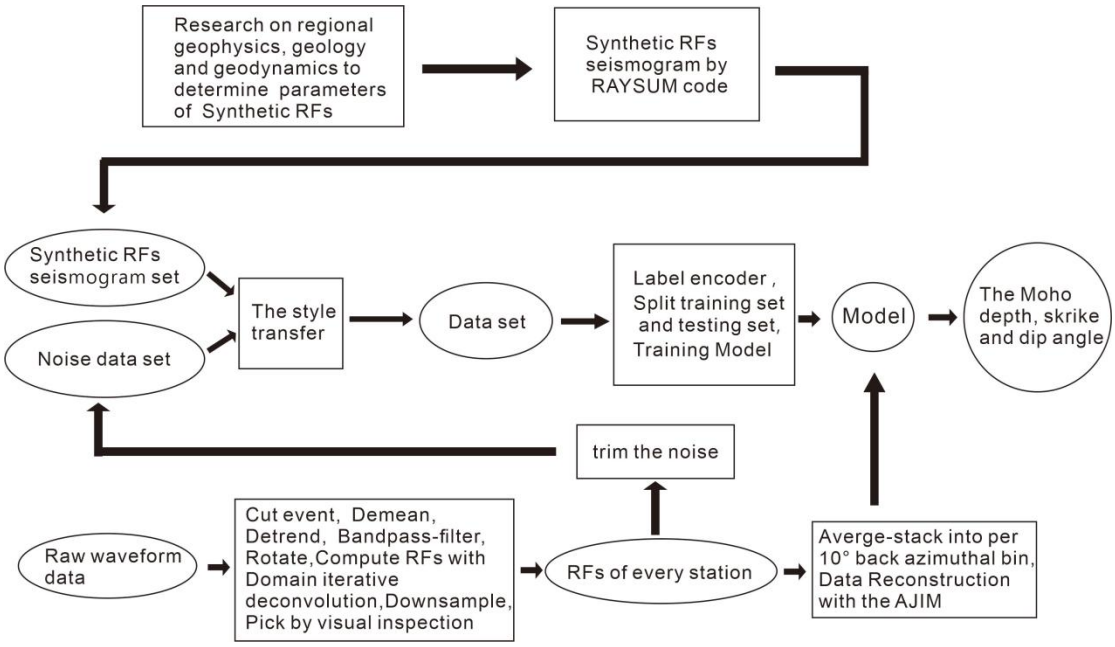

Figure 1. Workflow of the data processing scheme.

3.1 The synthetic RFs seismogram and labels encoded

The deep geological structures and the physical properties were carefully investigated and analyzed to retrieve the most appropriate design parameters for generating the synthetic data set. The crustal thickness range is from 26 to 43km (Wei et al., 2020), including a 0 to 3km low velocity sedimentary layer. Besides, the seismic imaging results show that the Moho of TLFZ and its adjacencies are relatively flat (Chen et al., 2006; Lü et al., 2015; Ma et al., 2020), so in the strike range of 0 to 360°, the dip angle range is set from 0 to 20°. In addition, considering wave velocity anisotropy in the crust, we randomly introduce 0 to 3% azimuthal anisotropy to every synthetic RFs seismogram (Bem et al., 2022; Gu et al., 2020). RFs are sensitive for wave velocity and density, hence, we set the average value of study areas as the initial parameters (Vp = 6.4km/s; Vs = 3.5km/s; The crustal density = 2800kg/m^3) (Luo et al., 2019; Pasyanos et.al. 2014; Zhang et al., 2020). Ultimately, 9000 synthetic RFs seismograms with a ray parameter of 0.06 s/km, each consisting of 36 RFs corresponding to 0 to 360° back azimuth, were produced by the RAYSUM code (Frederiksen & Bostock, 2000).

As mentioned above, the Moho depth was viewed as a classification task. We thus divided 26 to 43 km of crust thickness into one class per 1km. In practice, for instance, if the corresponding depth of one synthetic RFs seismogram is 34.76km, it will be rounded to 35. Next, all the depth labels of sample data were encoded by the one-hot. The Moho strike and dip angle were regarded as

two regression tasks, so the corresponding strike and dip angle of all synthetic RFs seismograms are normalized to -1 to 1.

3.2 The recombining synthetic RFs seismogram via the style transfer

A noise data set composed of 500 noise segments acted as a raw material of the style for attaining recombining synthetic RFs seismogram. First of all, we randomly selected an RF from the realistic RFs to be predicted and then trimmed a segment of 25s at any random time after 25s as one noise sample. Repeat this operation until 500 noisy samples were gathered as the noise set. After that, 36 noises were chosen randomly from the noise data set as the style, and a synthetic RFs seismogram with the same size acted as the content. Subsequently, we implemented the transfer style by a VGG19 net of pre-training on ImageNet excluding the three fully-connected layers at the top of the network (Fig. 2). The two wights of Formulae 4, and, were set toand, respectively. The research suggested that matching the content/style representation on layers played a vital role in the recombination (Gatys et al., 2016). therefore, we tried many combinations from different matching layers and evaluated their effect (Fig. S1 and Table S1). Finally, we matched the style features in layers block1_conv1, block2_conv1, block3_conv2, block4_conv2, and block5_conv2, whereas we matched the content features in layer block5_conv4 (Fig. S1b). In this case, the PSNR of the recombining RFs seismogram reached 26.22, and the SSIM reduced to 0.37 (Table S1). In the recombining RFs seismogram, the noises look exceedingly similar to these of realistic RFs seismograms. Although the amplitudes and arrivals of the conversions and the multiples were disturbed slightly, the overall structure of the waveform was still preserved (Fig. S1b), which was closer to the waveform characteristics of the real RFs. We processed all synthetic RFs seismograms via the style transfer to gain the data set for the next training step.

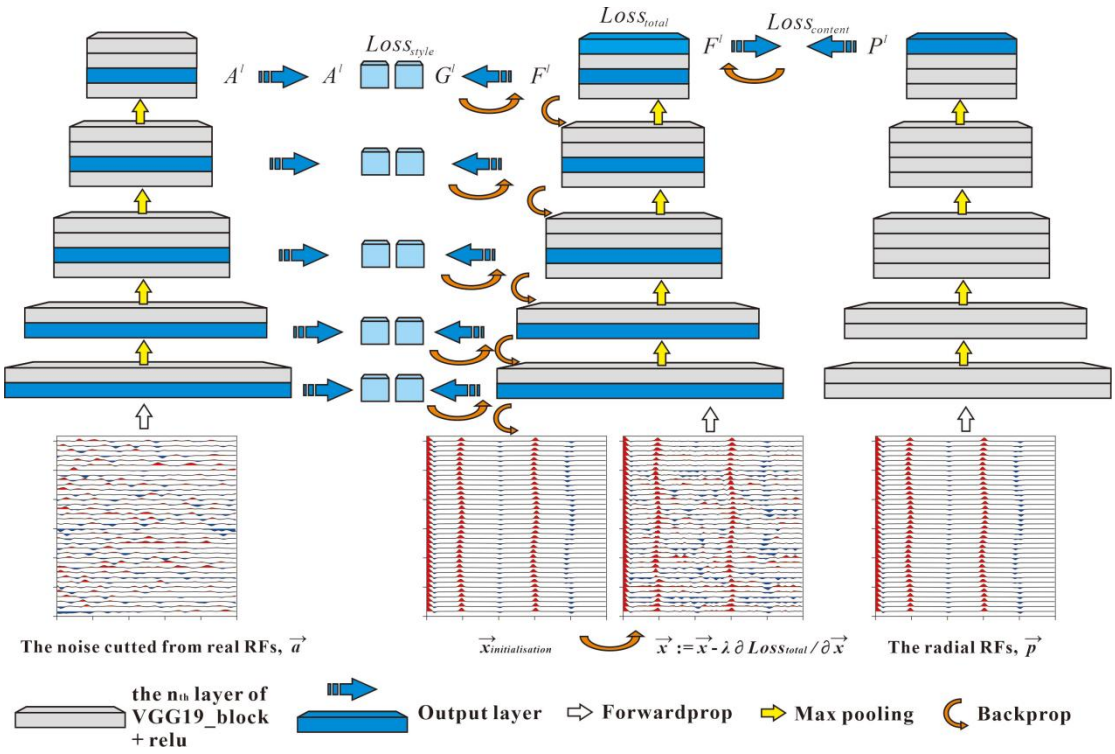

Figure 2. The style transfer process of the simulated synthetic RFs and the architecture of VGG-19. Modified from Gatys et al. (2016)

3.3 Architecture of the multitasking convolutional neural network

We built a multitasking convolutional neural network based on the hard parameter sharing. The network was comprised of a hard share bottom and three task-specific layers (Fig. 3). The hard share bottom contained three convolution layers with a rectified linear unit (ReLU) activation function. Furthermore, each layer was followed by a max pool to decrease the size of the convolved feature map. The input of the model was the recombining synthetic RFs seismogram with dimensions of 250 by 36 by 1, namely, the number of points per data component × the number of traces in the RFs seismogram × the number of channels (Fig. 3).

The three task-specific layers connected with the hard share bottom, and mainly consisted of many fully connected layers. The depth task layers and the dip angle task layers had a similar structure and shared the output of the hard share bottom after the flatten operation, which can reduce learning parameters and improve computing efficiency. As for the model in our case, the strike predictions were very crucial due to the inaccurate strike leading to meaningless occurrence representation although the dip angle was correctly constrained. Thus, the structure of the strike task layers was more complicated than the other task

layers, and we intentionally added a convolution layer and three additional fully connected layers and inserted two Batch Normalization in the last two layers. In all task-specific layers, we selected ReLU as the activation function in each layer except output layers. The depth task outputted the predicted result through Sigmoid, whereas two regression tasks outputted their predicted result through Hard-Tanh. Furthermore, L1_L2 class regularization for two regression tasks improved the model generalization by penalizing the coefficients effectively. The network needed to train a total of 169,990,720 parameters. Fig. 3 illustrated more details of the network.

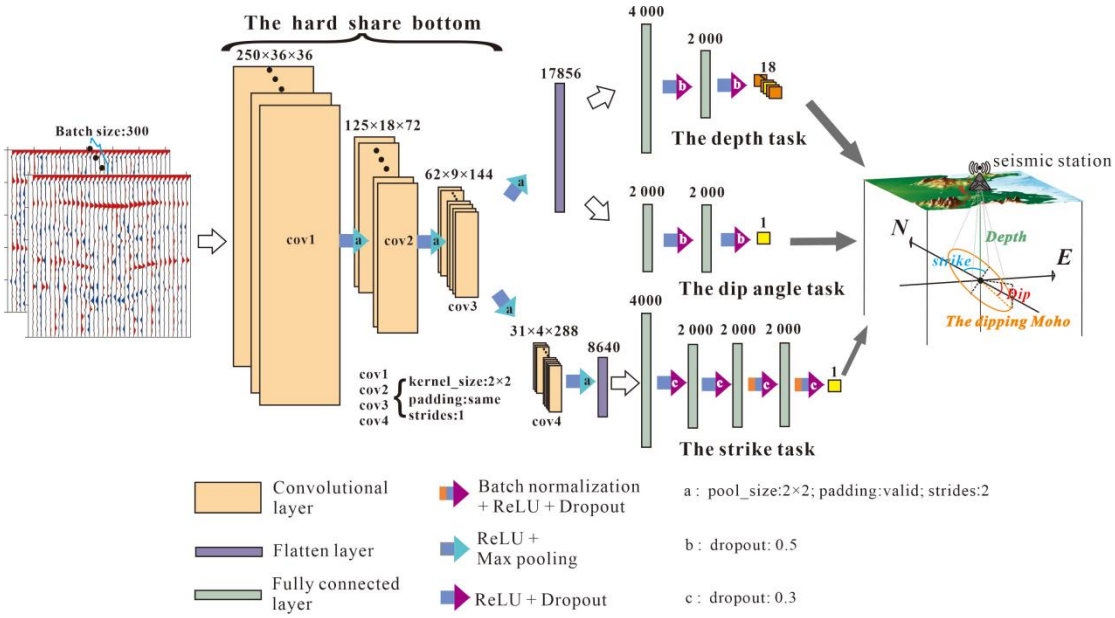

Figure 3. The architecture of the multitasking convolutional neural network. The hard share bottom on the left involves a key functional role in downsampling and extracting features; The three task-specific layers on the right are in charge of prediction of the Moho strike, dip angle, and depth, respectively.

4 Evaluation

To train the network, we utilized 32 epochs with a batch size of 300 and applied 20% of the training data as the validation data set in the training phase. The learning rate kept 0.001 at the first ten epochs, and then the learning rate scheduler became exponential decay as. The Adam algorithm was utilized to optimize the loss function.

With training operation, the training and validation loss curves declined at the first 10 epochs and then converged gradually(Fig. 4). The minimal gap between the two sets of curves implied that the loss was lower on the training data set than on the validation data set. The validation loss not curling upward obviously was an expecting sign that we are not facing an over-fitting problem. Since the

Moho depth prediction was a classification task, We preferred to evaluate the predictive effect with the accuracy. The good thing was that the accuracy ran up to above 90% after the 18th epoch, ultimately reaching 91.08% accuracy after the last epoch.

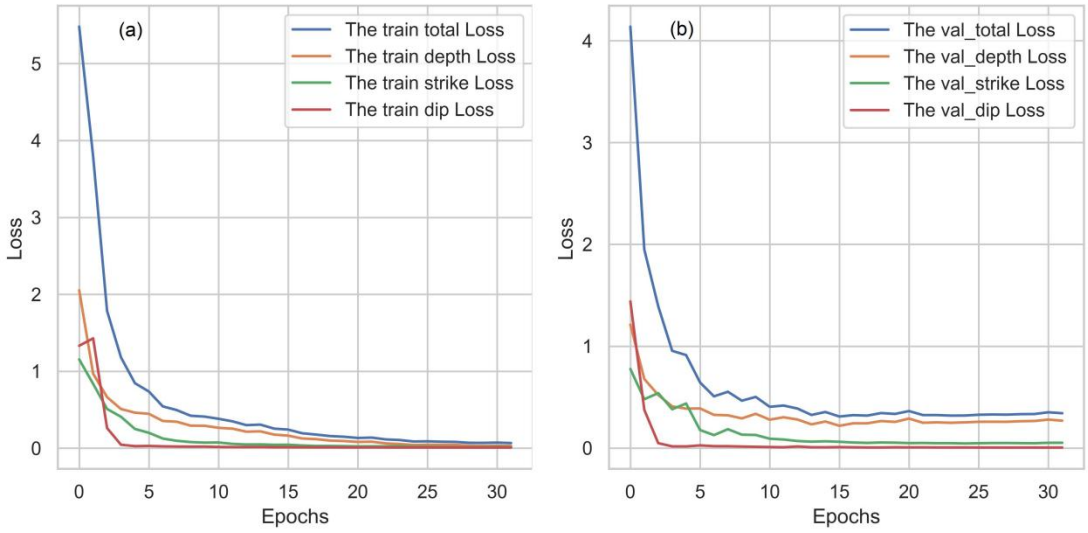

Figure 4. The training and validation loss curves for synthetic data. The strike loss curves (green) and the dip angle loss curves (red) were almost at the same lower level. The larger error coming from the depth loss curves (yellow) has affected the total loss curves (blue).

100 new samples as the test set were regenerated to evaluate the model performance further. The results were shown in Fig. 5a. 9 depth predictions deviate from the rounding label values. Notably, these errors barely are 1km, which indicates that the depth prediction is entirely acceptable, though the depth loss curve was less than ideal. Besides, the average error between the actual depth labels and the prediction was 0.289, which implied the prediction was also credible.

The 100 occurrence predictions were drawn in Fig. 5b. The mean error of the strike is 22.46°, and the mean error of the dip angle is 0.54°. In consideration that the actual Moho is a velocity interface with a complex structure, it permits us to elucidate the occurrence feature through a less precise strike and dip angle. For this reason, the 22.46° mean error is not too large for the back azimuth range of 0 to 360°.

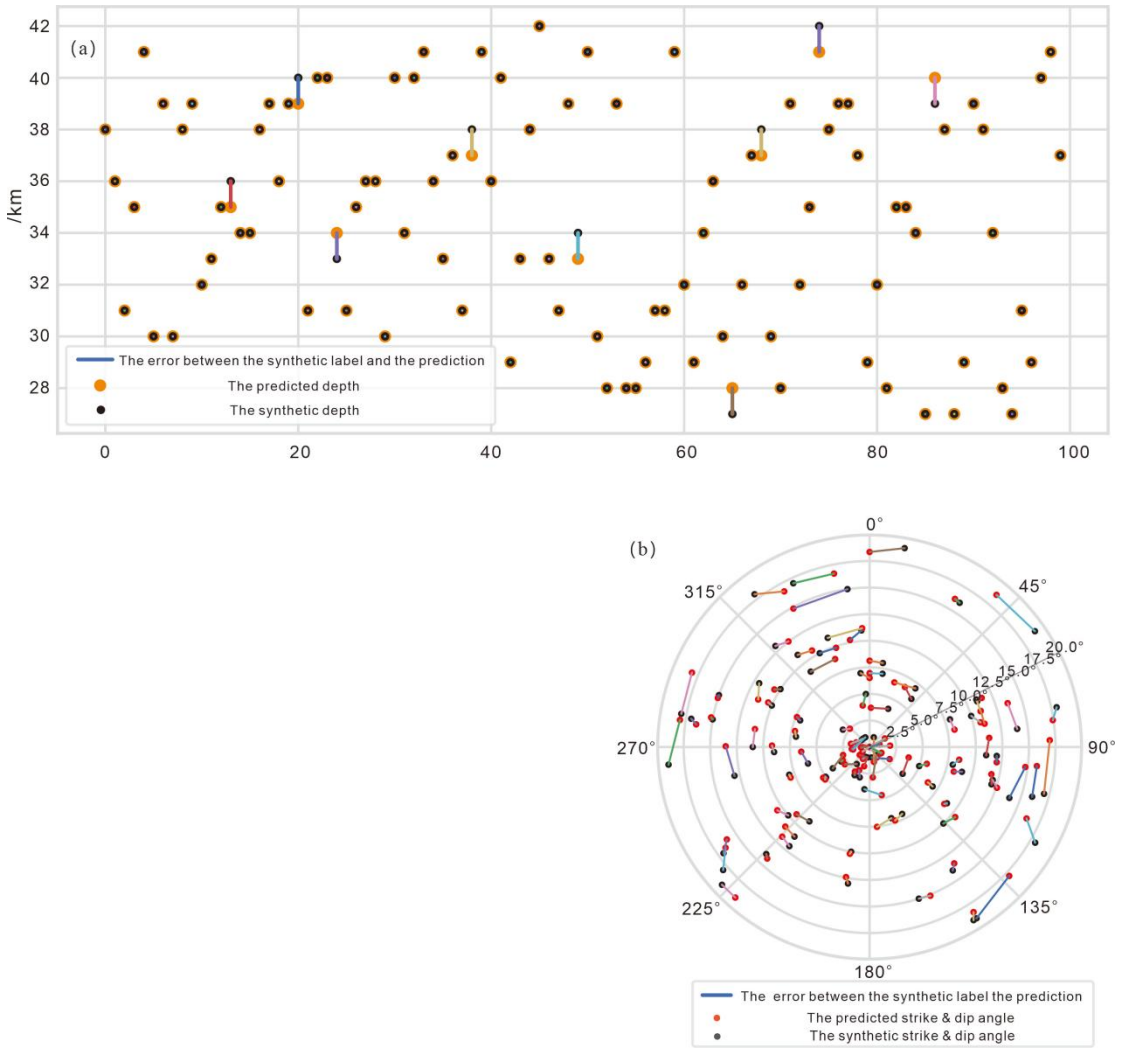

Figure 5. The comparison between the synthetic label and the prediction.

The colored lines represent error between the synthetic labels and the predictions of the Moho information.

4 Application

4.1 Geological settings

The current TLFZ is a gigantic sinistral strike-slip fracture zone in eastern China and acts as a connection between NCB and LYZB. Since Triassic, it has gone through several intense tectonic movements. Indonesian movement led to plate convergence and lithospheric thickening. While during the Yanshan movement period, with the Izanaqi plate retreated, the stress field of the East Asian Main-

land changed. The two-stage intense extension facilitated the development of many normal faults and rifted basins along the stress direction in TLFZ and its adjacencies (Zhang et al., 2003; Zhu et al., 2018), and contributed to lithosphere thinning over 120km and crustal deformation (Chen et al., 2006, 2014; Menzies et al., 1993; R. Zhu et al., 2012).

4.2 Data and Process

China earthquake administration established many permanent seismic stations equipped with broadband seismometers. These stations covered the study region well and recorded data throughout the year in a low-noise environment. We collected waveform data of seismic events (2013 to 2015) with magnitudes greater than Ms5.0 and epicentral distances ranging from 30° to 90° from 10 stations (PZ HBE HNA BEB SH HUA JAS CHZ MAS BAS), and computed radial RFs by time-domain iterative deconvolution (Ligorria & Ammon, 1999) with a Gaussian width of 2.5 and iteration number of 200 after the routine procedure (Demean; Detrend; Bandpass-filtered (0.02-2Hz); Rotate coordinate system (NEZ to RTZ); Moveout (0.06 s/km)). Then we discarded poor-quality RFs through visual inspection and preserved more than 300 records. Subsequently, the data of every station was average-stacked into per 10° back azimuthal bin and downsampled to 10Hz (eg. see Fig. 6a). Next, by setting the iteration number to 15, the scale to 4, and the angle to 16, all the RFs seismograms were reconstructed with the AJIM (eg. See Fig. 6b). The reconstructed RFs seismogram contained 250 sample points with 1 msec as the sampling interval along the time axis and 36 traces with 10° as the interval along the back azimuthal spatial direction. In the end, 10 seismograms as the prediction set were sent into the model one by one to output corresponding predicted results for further analysis.

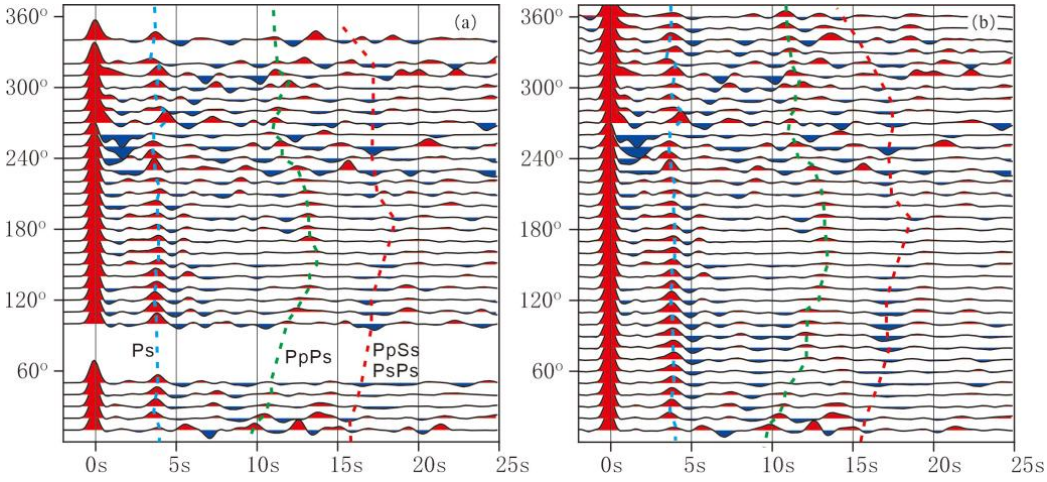

Figure 6. The realistic RFs seismogram and reconstructed RFs seismogram of BEB. In (a), the back azimuthal behavior of the conversions and the multiples are apparent and visible, whereas the missing traces are located in the back azimuthal range of 60° to 90° and 320° to 360°. In (b), the missing traces

can be reasonably recovered, and the Moho P-to-S converted phase and its the multiples can be clearly identified.

4.3 Result

The predicted Moho depth and occurrence below 10 stations are listed in Table 1, which reveals that the Moho depths are 32km on average and vary from 30 to 36km (Table 1 and Fig7). The crust of the area close to TLFZ (PZ, SH, JAS, CHZ, and BAS) is relatively thinner and not more than 34km. By way of contrast, the deepest Moho is below HNA, reaching 36km. The two neighboring stations, HNA and BEB, are located in the middle of the Hefei basin (Fig.7 see A), and their Moho depths are 35km and 30km correspondingly, which implies lateral inhomogeneity of regional crustal structure. HUA and MAS are situated on LYZB, and corresponding Moho depths are 30km and 32km, individually. To verify the reliability of the predicted depths, we comb the Moho depths from previous researches on TLFZ with the H-kappa method and the improved H-kappa method (Table 2). By comparison, our predicted depths are similar to the results computed by those conventional methods, some of which even show surprising consistency.

Most of the predicted strikes are near NE-SW, and the strikes of BAS, BEB, and MAS are near EW. BAS station is built on the intersection of three main tectonic units: NCB, LYZB, and the Dabie orogeny belt (Fig. 7 see D). Especially, the >40km crustal thickness of the Dabie orogeny belt could profoundly affect the Moho deformation of adjacent areas. MAS station is located in the Ningwu basin which is a part of the Yangtze River metallogenic belt (Fig. 7 see C) and develops a complex crustal structure. A previous study (Lü et al., 2015) revealed that a reflection structure called crocodile existed in the connection between the upper and lower crust below the Ningwu basin, indicating contraction takes an essential part in this formation of the crustal interior to a great extent. From our perspective, on the other hand, the Moho strikes beneath BAS, BEB, and MAS are most likely related to the second stage of Cretaceous extension, which we expand on the discussion in the next section.

The variation range of predicted dip angles is from 13 to 20°, which is different from previous results by other seismic imaging methods (Chen et al., 2006; Lü et al., 2015; Tian et al., 2020). Previously, scholars generally believed that the Moho below TFLZ is flat with low angle undulating. However, our predicted dip angles implied that the undulation is relatively more obvious. Amongst the predicted dip angles, the dip angles of JAS and CHZ are the largest (~20°), which is probably mainly affected by the evolution of the Zhangbaling uplift (Fig. 7 see B) except closer to TLFZ.

Table 1. The predictions and the fine tuned results

Results Station	Strike /°	Tuning Strike /°	Dip angle /°	Tuning dip angle /°	Depth /km

PZ
HBE
HNA
BEB
SH
HUA
JAS
CHZ
MAS
BAS

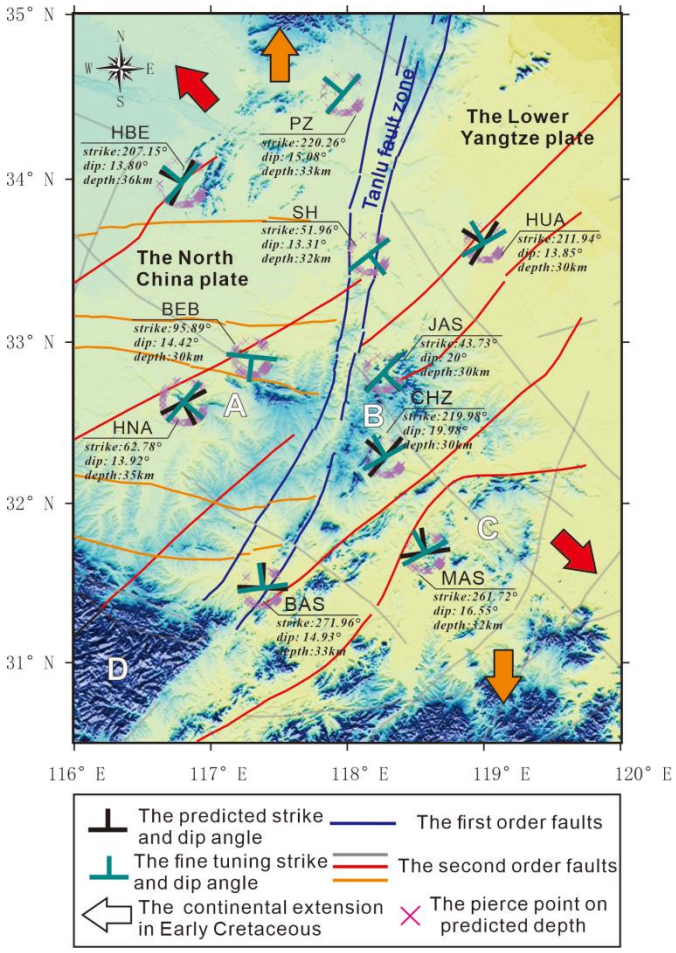

Figure 7. The predicted results and the sketch map of the tectonic setting. A, B, C, and D denote the Heifei basin, the Zhangbaling uplift, the Ningwu basin, and the Dabie orogeny belt in that order. The red lines and arrows represent

the faults and the stress orientation related to the first stage of continental extension in the earlier and middle Early Cretaceous, and the orange lines and arrows represent the faults and the stress orientation related to the second stage of continental extension in the late Early Cretaceous, respectively.

Table 2. The predictions in this paper and the depth results from other researches.

	Han et al., 2020 Han, 2020. *H-* /km	Wei et al., 2020. Multifrequency *H-* /km	Li et al., 2021. Two-layer *H-* /km	Chen et al., 2022. *H-* /km	Han et al., 2022. *H- -c* /km	This paper /km
PZ					-	
HBE						
HNA						
BEB						
SH		-				
HUA						
JAS						
CHZ						
MAS						
BAS						

4.4 Synthetic modeling and the fine tuning

The seismic imaging of the profile from conventional methods hardly provides accuracy validation to our predicted Moho occurrence. To verify the credibility of the results, we attempted to set predicted results as initial parameters of synthetic velocity model to observe whether the synthetic RFs seismogram was roughly the same as the reconstructive RFs seismogram. Considering the effect of unknown parameters, such as the wave velocity and anisotropy, we consulted relevant references to determine appropriate initial parameters as realistic as possible (Bem et al., 2022; Gu et al., 2020; Meng et al., 2019).

For better comparison, we performed synthetic modeling with two models: the non-tuning model and the tuning model. For the non-tuning model, the synthetic RFs seismograms were calculated in the case of the predicted results as initial parameters (Fig. 8b). In fact, most of the calculated synthetic RFs seismograms have presented high similarity with the reconstructed RFs seismogram, which indicated our predictions are relatively accurate. Whereas for the tuning model, we tuned more parameters including the predicted results, and performed again so that the synthetic RFs seismogram reached more similar features to the reconstructed RFs seismogram (Fig. 8c). We listed all tuned values of occurrence in Table 2, and displayed the synthetic modeling results of

HUA for it obtained the largest tuning efforts than other stations (Fig. 8).

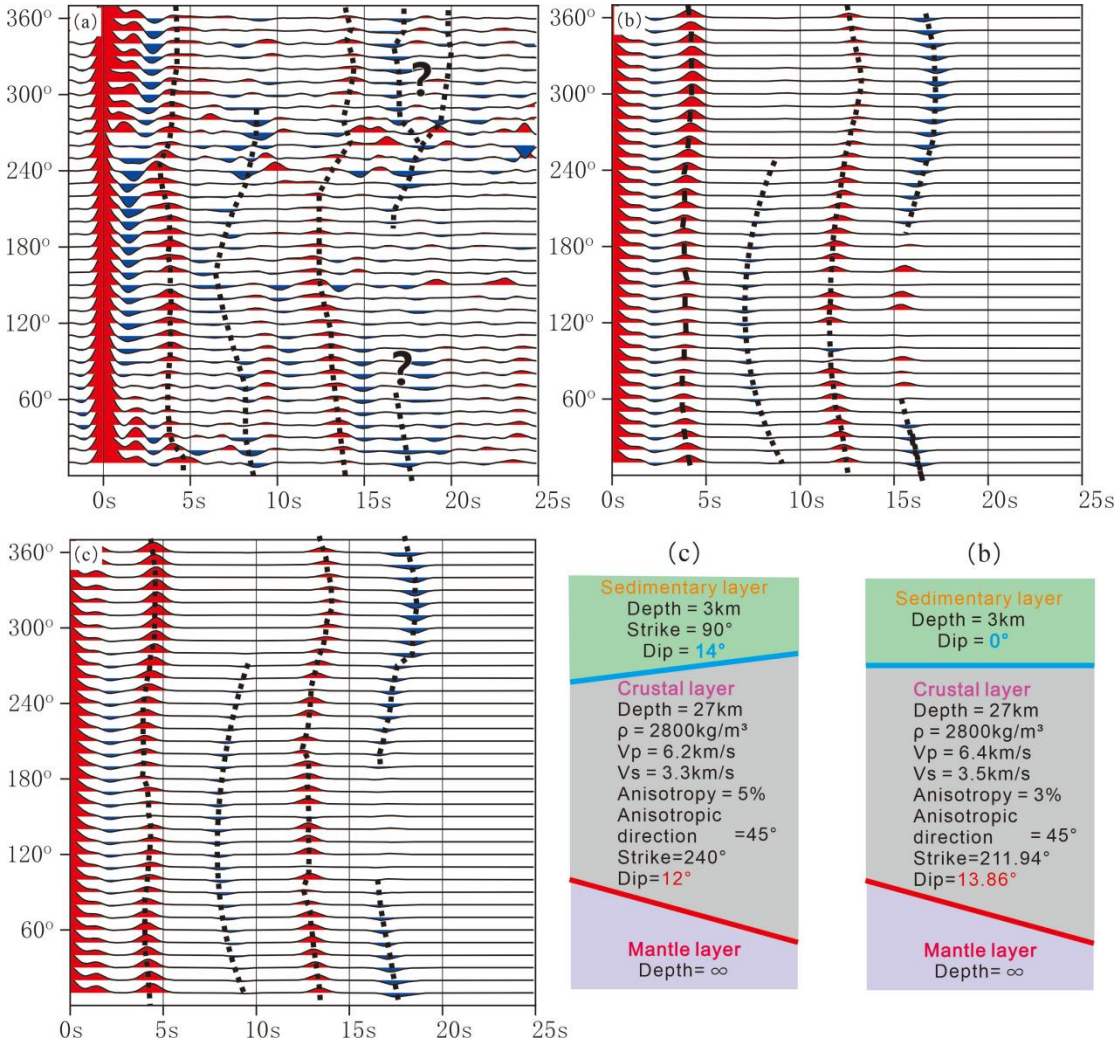

Figure 8. The comparison between the reconstructed RFs seismogram of HUA and the forward synthetic RFs seismogram.

1. is the reconstructed RFs seismogram. The arrangement of the interface phases is visible in their arrival time windows. Ps phase at around 4-5s is clear; PpPp phase is slightly visible in the time window of 5-10s. PpPs phase can be tracked continuously in the time window of 11-15s; A group of indistinct PsPs + PpSs phases seems complicated to be recognized precisely. (b) is the synthetic modeling RFs seismogram in the non-tuning model. We set the predictions as initial parameters for synthetic modeling, and estimate 3% azimuthal anisotropy with NE-striking in the velocity

model. (b) shows a similar phase structure on both the conversions and the multiples. We tune some parameters: the dip angle is reduced by nearly 2°, and the strike is increased by nearly 30°. To fit the phases, we assign 14° dip angle and 90° strike to the bottom of the sedimentary layer, and modify the crustal wave velocity and anisotropy appropriately. (c) shows that the synthetic RFs seismogram with fine tuning parameters is closer to (a) than (b), particularly in the sedimentary phases at 1-2s and PpPs phases at 11-15s.

5 Discussion

Bai & Wang. (2006) found that no apparent discrimination in velocity distribution and boundary topography exhibits in the lower crust below the two sides of TLFZ. Hence, it is inferred that the fault behavior in the lower crust had disappeared, while the fault features in the rigid middle-upper crust have been preserved up to the present. Furthermore, most seismic images presented a flat and low angle undulating Moho beneath TLFZ (Chen et al., 2006; Lü et al., 2015; Ma et al., 2020; Tian et al., 2020). Therefore, the current results from traditional seismic methods hardly established a connection between the lower crustal structure and the geological evolution.

G. Zhu et al. (2012; 2021) proved the principal extension direction evolved from WNW-ESE in the earlier and middle Early Cretaceous to NW-SE in the late Early Cretaceous. These two continental extensions are the most significant geological event during the period of the Yanshan movement, and also the reason for the lithospheric thinning and crustal deformation (Chen et al., 2006; Menzies et al., 1993). Thus, the intense multi-extension resulted in the reactivation of the great majority of normal faults accompanied by intensive magmatism. Eventually, two fault systems with different strikes developed along the stress field orientation in the middle-upper crust. Our predicted results unveil a significant coincidence: the predicted strikes are almost parallel with those of the most adjacent early Cretaceous normal faults (see Fig 7 labeled in red lines). That is to say, they are nearly perpendicular to the stress orientation during that period, which probably implies that the current crustal bottom structure preserves some tectonic properties related to the early Cretaceous extension. In other words, it seems to be indirect evidence that the stress field orientation of the major geological event has been recorded and preserved till now in lower crustal structures. The predicted 7 strikes (HBE, PZ, SH, JAS, HNA, HUA, and CHZ) almost perfectly parallel the nearest NE-striking normal faults, which can be viewed as a response to the stress field orientation of the first stage with intense activity occurring from 135-115 Ma since the early Cretaceous (Zhang et al., 2003; R. Zhu et al., 2012). The predicted strikes of BEB, MAS, and BAS are near EW-striking, which can be regarded as another response to the stress field orientation of the weaker second stage from 115-100Ma (Zhu et al., 2018).

The mantle-derived magma underplating and the partial melting of the lower crust are widely acknowledged as reasonable explanations when discussing the mechanism of the lower crustal deformation. Our views are not contradictory

to those classical theories as lower crustal deformation certainly depends on the interaction with deep heat flow to progress. Nevertheless, we pay more attention to how the extension affects the physical deformation of the lower crust. Reston. (1988) proposed lower crust boudinage as an answer to extension. Clerc et al. (2018) illustrated that the lower crust is often much weaker than previously thought, and its ductility shapes the representation of intensive extension. Their studies largely are in support of our opinion because the viscosity is a key to the deformation of the lower crust, while the composition, initial thermal state, and extension rate determine the viscosity (Huismans & Beaumont 2011, 2014; Brune et al., 2014). Nevertheless, there is no obvious boudinage tectonic below TLFZ and adjacencies since the evolutionary model of the back-arc extension (G. Zhu et al., 2012) is quite different from that of the rift breakup. The extension of the TLFZ manifested as a complex multi-stages process including an additional short-term compression, and was replaced by a sinistral strike-slip in round 100 Ma (G. Zhu et al., 2012).

We deduced the lower crustal deformation process of TLFZ and its adjacencies (Fig. 9). Till the early Cretaceous, the lithosphere below TLFZ and its adjacencies kept a structural feature of thickening (Fig. 9a). After that, the stress field began to transform since the rollback of the subducting Izanagi Plate, then immediately the intensive extension caused the lithosphere thinning and crustal deformation. Furthermore, many normal faults and rift basins developed along the extensional orientation in the brittle upper crust. By comparison, the ductile lower crust also had different responses to stress according to the differences of each regional composition. The high viscosity region kept its structural feature to a certain degree. In contrast, the low viscosity regions were under ongoing deformation in the lower crust (Fig. 9b). Ultimately, the lower crustal base of the middle-southern segment of TLFZ and its adjacencies present a tectonic feature of undulation at the end of the extension, and the tectonic strike is nearly parallel to the normal faults in the upper crust. We thus can regard these structures as extensional tectonics relics preserved in the crust.

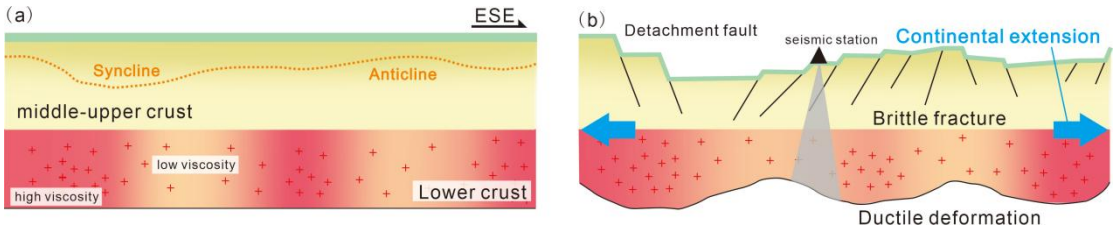

Figure 9. The lower crustal evolution of TLFZ and adjacencies in Cretaceous.

1. represents the tectonic state before the early Cretaceous, and (b) represents the lower crustal deformation process. The grey cone shape under the seismic station represents a rough predictive range. The density of red plus signs indicate the level of the lower crustal viscosity (the denser the red plus signs, the higher the regional viscosity, the weaker the ductile

deformation, and vice versa).

5 Conclusions

We propose a deep learning scheme to achieve the depth and occurrence of the Moho beneath the seismic stations. The scheme's core is using a multitasking convolutional neural network to learn the back azimuthal behavior of receiver functions seismogram. Based on the style transfer on convolutional neural network, we attain recombining synthetic RFs seismograms as the training set via 500 real noise data and 9000 synthetic RFs seismograms. Moreover, by introducing a data reconstruction method named the accelerated joint iterative method, we restore the RFs seismograms with missing traces in partial back azimuth.

By applying the newly proposed scheme to 10 broadband seismic data, we can elucidate the crust-mantle structure beneath the Tanlu fault zone (middle-southern segment) and its adjacencies in detail. The predictions unveil that bottom of the lower crust presents a structural behavior of undulation with near NE-striking. Furthermore, these deep tectonics, on the one hand, imply that intense continental extension can extensively affect the lower crustal deformation. On the other hand, it illustrates that the stress field orientation of the major geological event can be recorded and preserved in the lower crust.

Data Availability Statement

The raw data of the permanent seismic stations can be available by request through the the Data Management Centre of China National Seismic Network at the Institute of Geophysics, China Earthquake Administration (SEISDMC, https://doi.org/10.11998/SeisDmc/SN, http://www.seisdmc.ac.cn. Zheng et al., 2010). The P receiver functions waveforms and the model for this study can be downloaded at https://doi.org/10.11888/Geo.tpdc.271396 (Chen, 2021).

References

Bai, Z., & Wang. C. (2006). Crustal P-wave velocity structure in Lower Yangtze region: Reinterpretation of Fuliji-Fengxian deep seismic sounding profile. *Chinese Science Bulletin*. 51, 2391-2400. https://doi.org/10.1007/s11434-006-2115-z

Baxter, J. A. (1997). A Bayesian/Information theoretic model of learning to learn via multiple task sampling. *Machine Learning*. 28, 7-39. https://doi.org/10.1023/A:1007327622663

Bem, T. S., Liu, C., Yao, H., Luo, S., Yang, Y., & Liu, B. (2022). Azimuthally anisotropic structure in the crust and uppermost mantle in central East China and its significance to regional deformation around the Tan-Lu Fault zone. *Journal of Geophysical Research: Solid Earth*, 27, e2021JB023532. https://doi.org/10.1029/2021JB023532

Brune, S., Heine, C., Pérez-Gussinyé, M., Sobolev, S.V. (2014). Rift migration explains continental margin asymmetry and crustal hyper-

extension. *Nature Communications*, 5, 4014. https://doi.org/10.1038/ncomms5014

Candès, E. J., Demanet, L. (2004). The curvelet representation of wave propagators is optimally sparse. *Communications on Pure and Applied Mathematics*, 58(11), 1472-1528. https://doi.org/10.1002/cpa.20078

Caruana, R. A. (1993). Multitask learning: A knowledge-based source of inductive bias. *Machine Learning Proceedings*, 10(1), 41-48. https://doi.org/10.1016/B978-1-55860-307-3.50012-5

Chen, H. (2021). Crustal tectonic evolution of Tanlu fault zone (middle-southern segment) and adjacent areas under the background of extension: Evidences from teleseismic receiver functions. *National Tibetan Plateau Data Center*. https://doi.org/10.11888/Geo.tpdc.271396. CSTR: 18406.11.Geo.tpdc.271396.

Chen, H., Li, H., Hong D., Han. R., Wang, X., Deng, J., et al. (2022). Crustal tectonic evolution of Tanlu fault zone (southern segment) and adjacent areas under the background of extension:Evidences from teleseismic receiver function (in Chinese with English abstract). *Earth Science*. (Accept) https://kns.cnki.net/kcms/detail/42.1874.P.20220228.1853.013.html

Chen, L., Jiang, M., Yang, J., Wei, Z., Liu. C., & Ling. Y. (2014). Presence of an intralithospheric discontinuity in the central and western North China Craton: Implications for destruction of the craton. *Geology*, 42(3): 223-226. https://doi.org/10.1130/G35010.1

Chen, L., Wen, L., & Zheng, T. (2005). A wave equation migration method for receiver function imaging: 2. application to the Japan subduction zone. *Journal of Geophysical Research: Atmospheres*, 110, B11310. https://doi.org/10.1029/2005JB003666

Chen, L., Zheng, T., & Xu, W. (2006). A thinned lithospheric image of the Tanlu Fault Zone, eastern China: Constructed from wave equation based receiver function migration. *Journal of Geophysical Research: Solid Earth*, 111, B09312. https://doi.org/10.1029/2005JB003974

Clerc, C., Ringenbach, J. C., Jolivet. L., & Ballard, J. F. (2018). Rifted margins: Ductile deformation, boudinage, continentward-dipping normal faults and the role of the weak lower crust. *Gondwana Research*, 53, 20-40. http://doi.org/10.1016/j.gr.2017.04.030

Dalai, B., Kumar, P., Srinu, U., & Sen M. K. (2022). De-noising receiver function data using the unsupervised deep learning approach. *Geophysical Journal International*, 229, 737-749. https://doi.org/10.1093/gji/ggab494

Donoho, D. L. (2006). Compressed sensing. *IEEE Transactions on Information Theory*, 52(4), 1289-1306. https://doi.org/10.1109/TIT.2006.871582

Frederiksen, A. W.,& Bostock, M. G. (2000). Modelling teleseismic waves in dipping anisotropic structures. Geophysical Journal International, 141(2), 401-412. https://doi.org/10.1046/j.1365-246x.2000.00090.x

Gatys, L. A., Ecker, A. S., & Bethge, M. (2016). Image Style Transfer Using Convolutional Neural Networks. *2016 IEEE Conference on Computer Vision and Pattern Recognition (CVPR).* https://doi.org/10.1109/CVPR.2016.265

Gan, L., Wu, Q. J., Huang, Q., & Tang, R. (2021). Quick selection of receiver function based on convolutional neural network (in Chinese with English abstract). *Chinese Journal of Geophysics*, 64(7): 2394-2404. https://doi.org/10.6038/cjg2021O0141

Gou, F.Y., Liu, C., Liu, Y., Feng, X., & Cui, F. (2014). Complex seismic wavefield interpolation based on the Bregman iteration method in the sparse transform domain. *Applied Geophysics*, 11(3), 277-288. https://doi.org/10.1007/s11770-014-0443-3

Gu, Q., Kang, Q., Zhang P., Meng Ke., Wu S., Li Z., et al. (2020). Rayleigh wave phase velocity and azimuthal anisotropy of the middle-southern segment of the Tan-Lu fault zone and adjacent regions from ambient noise tomography (in Chinese with English abstract). *Seismology and Geology*, 42(5), 1129-1152. https://doi.org/10.3969/j.issn.0253-967.2020.05.007

Han, R. (2020). Morphology and multisphere coupling of crustal and upper mantle discontinuities beneath Southeastern China. (Doctoral dissertation). Retrieved from CNKI.(https://kns.cnki.net/kcms/detail/detail.aspx?dbcode=CDFD&dbname=CDFDLAST2022&filena
s4JHMr6kS4h6pgwJabMVNDwXokCK1j5nyHXcmLVF6UNrsAlosY6mpyk).
Wuhan: China University of Geosciences.

Han, R., Li, Q., Huang, R., & Zhang, H. (2020). Detailed structure of mantle transition zone beneath southeastern China and its implications for thinning of the continental lithosphere. *Tectonophysics*, 789, 228480. https://doi.org/10.1016/j.tecto.2020.228480

Han, R., Yang, D., Li, Q., Chen, H., Zhang, H., Ye, Z., et al. (2022). Crustal structure and anisotropy in the Lower Yangtze region and its metallogenic implications. *Frontiers Earth Science*, 10, 849088. https://doi.org/10.3389/feart.2022.849088

Huang, B., Ma, S., & Goldfarb, D. (2013). Accelerated Linearized Bregman Method. *Journal of Scientific Computing*, 54, 428-453.

https://doi.org/10.1007/s10915-012-9592-9

Huismans, R.S., & Beaumont, C. (2011). Depth-dependent extension, two-stage breakup and cratonic underplating at rifted margins. *Nature*. 473, 74-78. http://doi.org/10.1038/nature09988

Huismans, R. S., & Beaumont, C. (2014). Rifted continental margins: the case for depth-dependent extension. *Earth and Planetary Science Letters*, 407, 148-162. http://doi.org/10.1016/j.epsl.2014.09.032

Jia, L., Mo, X., Santosh, M., Yang, Z., Yang, D., Dong, G., et al. (2016). Early Cretaceous continental delamination in the Yangtze Block: Evidence from high-Mg adakitic intrusions along the Tanlu fault, central Eastern China. *Journal of Asian Earth Sciences*, 127, 152-169. https://doi.org/10.1016/j.jseaes.2016.06.001.

Kang, Y., Shi, Y., & Anderson, J.L. (2021). Tectonic mechanism and evolution of eastern China during the Early Cretaceous: a view from magmatism in the middle to Southern Tan-Lu fault zone, *International Geology Review*, 63(1), 21-46. https://doi.org/10.1080/00206814.2019.1700400

Kosarev, G., Kind, R., Sobolev, S.V., Yuan X. H., Hanka, W., & Oreshin. S. (1999). Seismic Evidence for a Detached Indian Lithospheric Mantle Beneath Tibet. *Science*. 283(5406), 1306-1309. https://doi.org/10.1126/science.283.5406.1306

Langston, C. A. (1977). The effect of planar dipping structure on source and receiver responses for constant ray parameter. *Bulletin of the Seismological Society of America*, 67(4), 1029-1050.

Lei, J., Zhao, D., Xu, X., Du, M., & Lu, M. (2020). P-wave upper-mantle tomography of the tanlu fault zone in eastern china. *Physics of The Earth and Planetary Interiors*, 299, 106402. https://doi.org/10.1016/j.pepi.2019.106402

Li, J., Song, X., Wang, P., & Zhu, L. (2019). A generalized H-method with harmonic corrections on Ps and its crustal multiples in receiver functions.*Journal of Geophysical Research: Solid Earth*, 124. https://doi.org/10.1029/2018JB016356

Li, L., Shen, W., Sui. S., Yao, H., & Bao, Z. (2021). Crustal thickness beneath the Tanlu fault zone and itstectonic significance based on two-layer H- stacking. *Earthquake Science*, 34(3), 199-210. https://doi.org/10.29382/eqs-2020-0064

Li, Z., Tian, Y., Zhao, P., Liu, C., & Li, H. (2021). Receiver functions auto-picking method on the basis of deep learning (in Chinese with English abstract). *Chinese Journal of Geophysics* (in Chinese), 64(5), 1632-1642. https://doi.org/10.6038/cjg2021O0378

Ligorria, J. P., & Ammon, C. J. (1999). Iterative deconvolution and receiver-function estimation. *Bulletin of the Seismological Society of America*, 89, 1395-1400.

Liu, H., & Niu F. (2012). Estimating crustal seismic anisotropy with a joint analysis of radial and transverse receiver function data. *Geophysical Journal International*, 188, 144-164. https://doi.org/10.1111/j.1365-246X.2011.05249.x

Luo, S., Yao, H., Li, Q., Wang, W., Wan, K., Meng, Y., et al. (2019). High-resolution 3D crustal S-wave velocity structure of the Middle-Lower Yangtze River Metallogenic Belt and implications for its deep geodynamic setting. Science China Earth Sciences, 62, 1361-1378, https://doi.org/10.1007/s11430-018-9352-9

Lü, Q., Shi, D., Liu, Z., Zhang, Y., Dong, S., & Zhao, H. (2015). Crustal structure and geodynamics of the Middle and Lower reaches of Yangtze metallogenic belt and neighboring areas: Insights from deep seismic reflection profiling. *Journal of Asian Earth Sciences*, 114(4), 704-716. https://doi.org/10.1016/j.jseaes.2015.03.022

Ma, C., Lei, J., & Xu. X. (2020). Three-dimensional shear-wave velocity structure under the Weifang segment of the Tanlu fault zone in eastern China inferred from ambient noise tomography with a short-period dense seismic array. *Physics of the Earth and Planetary Interiors*, 309, 106590. https://doi.org/10.1016/j.pepi.2020.106590

McNamara, D. E., & Owens, T. J. (1993). Azimuthal shear wave velocity anisotropy in the basin and range province using moho ps converted phases. *Journal of Geophysical Research*, 98(B7), 12003-12017. https://doi.org/10.1029/93JB00711

Meng, Y., Yao, H., Wang, X., Li L., Feng J., Hong D., et al. (2019). Crustal velocity structure and deformation features in the central-southern segment of Tanlu fault zone and its adjacent area from ambient noise tomography(in Chinese with English abstract). *Chinese Journal of Geophysics*, 62(7), 2490-2509. https://doi.org/10.6038/cjg2019M0189

Menzies, M., Fan, W., & Zhang. M. (1993). Palaeozoic and Cenozoic lithoprobe and the loss of >120 km of Archean lithosphere, Sino-Korean Craton, China. *Geological Society.* 76(1), 71-81. http://dx.doi.org/10.1144/GSL.SP.1993.076.01.04

Millet, F., Bodin, T., & Rondenay, S. (2019). Multimode 3-D Kirchhoff migration of receiver functions at continental scale. *Journal of Geophysical Research: Solid Earth*, 124(8), 8953-8980. https://doi.org/10.1029/2018JB017288

Monsalve, G., Jaramillo, J. , Cardona, A., Schulte-Pelkum,

V., Posada, G., Valencia, V. et al. (2019). Deep crustal faults, shear zones, and magmatism in the Eastern Cordillera of Colombia: Growth of a plateau from teleseismic receiver function and geochemical Mio-Pliocene volcanism constraints. *Journal of Geophysical Research: Solid Earth*, 124, 9833-9851. https://doi.org/10.1029/2019JB017835

Nagaya, M., Oda, H., Akazawa, H., & Ishise, M. (2008). Receiver Functions of Seismic Waves in Layered Anisotropic Media: Application to the Estimate of Seismic Anisotropy. *Bulletin of the Seismological Society of America*, 98(6), 2990-3006. https://doi.org/10.1785/0120080130

Osher, S., Burger, M., Goldfarb, D., Xu, J., & Yin,W. (2005). An iterative regularization method for total variation-based image restoration. *Multiscale Modeling and Simulation*, 4(2), 460-489. https://doi.org/10.1137/040605412

Pasyanos, M. E., Masters, T., Laske G., & Ma, Z. (2014). LITHO1.0: An updated crust and lithospheric model of the Earth, *Journal of Geophysical Research: Solid Earth*, 119, 2153-2173, https://doi.org/10.1002/2013JB010626

Peng, X., & Humphreys, E.D. (1997). Moho dip and crustal anisotropy in northwest Nevada from teleseismic receiver functions, *Bulletin of the Seismological Society of America*, 87(3),745-754. https://doi.org/10.1785/BSSA0870030745

Reston, T.J., (1988). Evidence for shear zones in the lower crust offshore Britain. Tectonics, 7, 929-945. http://doi.org/10.1029/TC007i005p00929

Savage, M. K. (1998). Lower crustal anisotropy or dipping boundaries? effects on receiver functions and a case study in New Zealand. *Journal of Geophysical Research.* 103, B7:15069-15087. https://doi.org/10.1029/98JB00795

Sherrington, H. F., Zandt, G., & Frederiksen A.W. (2004), Crustal fabric in the Tibetan Plateau based on waveform inversions for seismic anisotropy parameters. Journal of Geophysical Research: Solid Earth, 109, B02312. https://doi.org/10.1029/2002JB002345

Shi, D., Lü Q., Xu, W., Yan, J., Zhao. J., Dong. S., et al. (2013). Crustal structure beneath the middle-lower Yangtze metallogenic belt in East China:Constraints from passive source seismic experiment on the Mesozoic intra-continental mineralization. *Tectonophysics*, 606, 48-59. https://doi.org/10.1016/j.tecto.2013.01.012

Tian, F., Lei, J., & Xu, X., (2020). Teleseismic P-wave crustal tomography of the Weifang segment on the Tanlu fault zone: A

case study based on short-period dense seismic array experiment. *Physics of the Earth and Planetary Interior*, 306, 106521. https://doi.org/10.1016/j.pepi.2020.106521

Shen, X., Liu, M., Gao, Y., Wang, W., Shi, Y., An, M., et al. (2017). Lithospheric structure across the northeastern margin of the Tibetan Plateau: Implications for the plateau's lateral growth. *Earth and Planetary Science Letters*, 459, 80-92. https://doi.org/10.1016/j.epsl.2016.11.027

Ruder, S. (2017). An Overview of Multi-Task Learning in Deep Neural Networks. *arXiv preprint arXiv*, 1706.05098

Wang, F., Song, X., & Li, J. (2022). Deep learning-based H- method (HkNet) for estimating crustal thickness and Vp/Vs ratio from receiver functions. *Journal of Geophysical Research: Solid Earth*, 127, e2022JB023944. https://doi.org/10.1029/2022JB023944

Wang, P., Suo, Y., Cao, X., Zhu, J., Hui, G., & Wang, G. (2021). Late Cretaceous-Cenozoic cooling of the southern Lower Yangtze river area: a response to subduction of the izanagi and pacific plates. *Gondwana Research*, 102, 31-45. https://doi.org/10.1016/j.gr.2021.02.016

Wei, Z., Chu, R., Chen, L., & Wu, S. (2020). Crustal structure in the middle-southern segments of the Tanlu Fault Zone and adjacent regions constrained by multifrequency receiver function and surface wave data. *Physics of The Earth and Planetary Interiors*, 301(4), 106470. https://doi.org/10.1016/j.pepi.2020.106470

Wirth, E. A. , & Long, M. D. (2013). Multiple layers of seismic anisotropy and a low-velocity region in the mantle wedge beneath Japan: evidence from teleseismic receiver functions. *Geochemistry Geophysics Geosystems*, 13(8), 1525-2027. https://doi.org/10.1029/2012GC004180

Yang, T., Cao, D., Du, N., Cui, R., Nan F., Xu Y., et al. (2022). Prediction of shear-wave velocity using receiver functions based on the deep learning method(in Chinese with English abstract). Chinese Journal of Geophysics, 65(1), 214-226. https://doi.org/10.6038/cjg2022P0025

Ye, Z., Gao, R., Li, Q., Zhang. H, Shen, X., & Liu, X. (2015). Seismic evidence for the North China plate underthrusting beneath northeastern Tibet and its implications for plateau growth. Earth and Planetary Science Letters, 426, 109-117. https://doi.org/10.1016/j.epsl.2015.06.024

Ye, Z., Li, Q., Zhang H., Li. J.,Wang, X., Han, R., et al. (2019). Crustal and uppermost mantle structure across the Lower Yangtze

region and its implications for the late Mesozoic magmatism and metallogenesis,eastern South China. *Physics of the Earth and Planetary Interiors*, 297, 106234. https://doi.org/10.1016/j.pepi.2019.106324

Yin, H., Zhu, G.,Wu, X., Su, N., Lu, Y., & Zhang, S. (2020). Continental response to mid-Cretaceous global plate reorganization: Evidence from the Tan-Lu Fault Zone, eastern China. *Gondwana Research*. 86, 23-45. https://doi.org/10.1016/j.gr.2020.05.005

Zhao, T., Zhu, G., Lin, S., Yan. L.,& Jiang, Q. (2014). Protolith ages and deformation mechanism of metamorphic rocks in the Zhangbaling uplift segment of the Tan-Lu Fault Zone. *Science China Earth Sciences*. 57, 2740-2757. https://doi.org/10.1007/s11430-014-4959-4

Zhang J., Chen L., & Wang X. (2019). Crustal structure study based on principal component analysis of receiver functions. *Science China Earth Sciences*. 62(7), 15. https://doi.org/10.1007/s11430-018-9341-9

Zhang, J., & Langston, C. A. (1995). Dipping structure under Dourbes, Belgium, determined by receiver function modeling and inversion. *Bulletin of the Seismological Society of America*, 85(1), 254-268. https://doi.org/10.1785/BSSA0850010254

Zhang, H., Liang. S., Peng, Q., Pang. Y., Jiang. Y., & Song, W. (2022). Separation of simultaneous source data via an accelerated joint iterative method.*Journal of Applied Geophysics*, 203, 104680. https://doi.org/10.1016/j.jappgeo.2022.104680

Zhang, H., Wang, D., Li, H., Huang, G., & Chen X. (2017). High accurate seismic data reconstruction based on non-uniform curvelet transform (in Chinese with English abstract). *Chinese Journal of Geophysics*, 60(11), 4480-4490. https://doi.org/10.6038/cjg20171132

Zhang, Y., Ma, Y., Yang N., Shi, Wei., & Dong, S., (2003). Cenozoic extensional stress evolution in North China. 36(5), 591-613. https://doi.org/10.1016/j.jog.2003.08.001

Zhang, Y., Wang, B., Xu, T., Yang, W., Wang, W., Xu Y., et al. (2020). Three-dimensional crustal Vp and Vs structures beneath the southern segment of the tan-lu fault revealed by active source and earthquake data. *Geophysical Journal International*, 223, 2148-2165. https://doi.org/10.1093/gji/ggaa314

Zheng, Y., Xu, Z., Zhao, Z., & Dai, L. (2018). Mesozoic mafic magmatism in North China: Implications for thinning and destruction of cratoniclithosphere. *Science China Earth Sciences*, 61, 353-385. https://doi.org/10.1007/s11430-017-9160-3

Zheng, X., Yao, Z., Liang, J., & Zheng, J., (2010). The role played and opportunities provided by IGP DMC of China National Seismic Network in Wenchuan earthquake disaster relief and researches. *Bulletin of the Seismological Society of America*. 100(5B), 2866-2872. https://doi.org/10.1785/0120090257

Zhu, L. P. (2000). Crustal structure across the San Andreas Fault, Southern California from teleseismic converted waves. *Journal of Geophysical Research: Solid Earth*.179(1):183-190. https://doi.org/10.1016/S0012-821X(00)00101-1

Zhu, L. P., & Kanamori, H. (2000). Moho depth variation in southern California from teleseismic RFs. *Journal of Geophysical Research: Atmospheres*, 105(B2), 2969-2980. https://doi.org/10.1029/1999JB900322ornia from teleseismic converted waves. *Earth and Planetary Science Letters*, 179(1), 183-190. https://doi.org/10.1016/S0012-821X(00)00101-1

Zhu, G., Jiang, D. Z., Zhang, B. L.,& Chen, Y. (2012). Destruction of the eastern North China Craton in a backarc setting: Evidence from crustal deformation kinematics. *Gondwana Research*, 22, 86-103. https://doi.org/10.1016/j.gr.2011.08.005

Zhu, G., Liu, C., Gu, C., Zhang, S., Li, Y., Su, N., et al. (2018). Oceanic plate subduction history in the western Pacific Ocean: Constraint from late Mesozoic evolution of the Tan-Lu Fault Zone. *Science China Earth Sciences*, 61, 386-405, https://doi.org/10.1007/s11430-017-9136-4

Zhu, G., Lu, Y., Su, N., Wu, X., Yin, H., Zhang, S., et al (2021). Crustal deformation and dynamics of Early Cretaceous in the North China Craton.Science China Earth Sciences, 64(9), 1428-1450. https://doi.org/10.1007/s11430-020-9749-0

Zhu, R., Xu, Y., Zhu, G., Zhang, H., Xia, Q.,& Zheng T. (2012). Destruction of the North China Craton. *Science China Earth Sciences*, 55, 1565-1587. https://doi.org/10.1007/s11430-012-4516-y